Atmospheric Environment 290 (2022) 119367

Contents lists available at ScienceDirect

Atmospheric Environment

journal homepage: www.elsevier.com/locate/atmosenv

NO_2 retrievals from NOAA-20 OMPS: Algorithm, evaluation, and observations of drastic changes during COVID-19

Xinzhou Huang [a], Kai Yang [a,*], Shobha Kondragunta [b], Zigang Wei [c], Lukas Valin [d], James Szykman [e], Mitch Goldberg [b]

[a] Department of Atmospheric and Oceanic Science, University of Maryland, College Park, MD, USA
[b] NOAA NESDIS, College Park, MD, USA
[c] IMSG at NOAA, College Park, MD, USA
[d] US EPA, ORD, Center for Environmental Measurements and Modeling, Research Triangle Park, NC, USA
[e] US EPA, ORD, Center for Environmental Measurements and Modeling, Hampton, VA, USA

HIGHLIGHTS

- Daily global NO_2 distribution can be mapped by NOAA-20 OMPS measurements.
- NOAA-20 OMPS detects a large decline (20–40%) of tropospheric NO_2 due to COVID-19 lockdown.
- OMPS tropospheric NO_2 correlates well with ground-based Pandora measurements.
- OMPS stratospheric NO_2 agrees excellently with OMI observations.

ARTICLE INFO

Keywords:
NOAA-20
OMPS
Stratosphere and troposphere NO2
COVID-19

ABSTRACT

We present the first NO_2 measurements from the Nadir Mapper of Ozone Mapping and Profiler Suite (OMPS) instrument aboard the NOAA-20 satellite. NOAA-20 OMPS was launched in November 2017, with a nadir resolution of 17 × 13 km^2 similar to the Ozone Monitoring Instrument (OMI). The retrieval of NOAA-20 NO_2 vertical columns were achieved through the Direct Vertical Column Fitting (DVCF) algorithm, which was uniquely designed and successfully used to retrieve NO_2 from OMPS aboard Suomi National Polar-orbiting Partnership (SNPP) spacecraft, predecessor to NOAA-20. Observations from NOAA-20 reveal a 20–40% decline in regional tropospheric NO_2 in January–April 2020 due to COVID-19 lockdown, consistent with the findings from other satellite observations. The NO_2 retrievals are preliminarily validated against ground-based Pandora spectrometer measurements over the New York City area as well as other U.S. Pandora locations. It shows OMPS total columns tend to be lower in polluted urban regions and higher in clean areas/episodes associated with relatively small NO_2 total columns, but generally the agreement is within ±2.5 × 10^{15} molecules/cm^2. Comparisons of stratospheric NO_2 columns exhibit the excellent agreement between OMPS and OMI, validating OMPS capability in capturing the stratospheric background accurately. These results demonstrate the high sensitivity of OMPS to tropospheric NO_2 and highlight its potential use for extending the long-term global NO_2 record.

1. Introduction

Nitrogen dioxide (NO_2) is a major air pollutant in the troposphere with varying levels of regulatory standards for ambient concentrations across the world. Its prevalence contributes to other secondary air pollutant formation, such as tropospheric ozone and nitrate aerosols, which are consequently harmful to human health and climate (Lelieveld et al., 2015; Seinfeld and Pandis, 2016). The primary sources of nitrogen oxides (NO_x = NO_2 + NO) are anthropogenic, produced mostly by combustion processes, with the rest being natural sources from fires, lightning, and soils. Due to the short photochemical lifetime of NO_2, which varies from ~2-6 h in summer to ~12–27 h in winter (Beirle et al.,

* Corresponding author.
E-mail address: kaiyang@umd.edu (K. Yang).

https://doi.org/10.1016/j.atmosenv.2022.119367
Received 29 April 2022; Received in revised form 10 August 2022; Accepted 29 August 2022
Available online 5 September 2022

2011; Laughner and Cohen, 2019; Shah et al., 2020), tropospheric NO_2 concentrations are spatially correlated with local NO_x emissions at spatial scales of ~10 km (Beirle et al., 2019). The atmospheric chemistry community has been using satellite observations since the mid-1990s to monitor daily global NO_2 loading, investigate long-term trends and short-term NO_2 changes, and locate NO_x emission sources to aid control policy strategies (Duncan et al., 2016; Lin et al., 2019).

The ongoing COVID-19 pandemic has caused unprecedented societal and economic impact worldwide. Satellite observations show a drastic decline in tropospheric NO_2 vertical column density over China following the outbreak of COVID-19, reflecting reduced fossil fuel usage due to decreases in economic activity and restrictions on travel (Huang and Sun, 2020; Liu et al., 2020). Similar declines have also been seen over Italy (Bauwens et al., 2020), India (ESA, 2020), North America (Goldberg et al., 2020; Kondragunta et al., 2021; Tzortziou et al., 2021) as observed by the TROPOspheric Monitoring Instrument (TROPOMI) and the Ozone Monitoring Instrument (OMI). These satellite-based studies illustrate the importance of spaceborne observations for providing timely and continuous air quality monitoring.

The OMPS Nadir Mapper aboard the NOAA-20 satellite was launched in November 2017, which is a successor to OMPS aboard Suomi National Polar-orbiting Partnership (SNPP) satellite under the NOAA/NASA Joint Polar Satellite Systems (JPSS) mission. The JPSS mission provides OMPS in orbit to the 2040s, extending the long-term record of many atmospheric trace gases, including O_3, SO_2 and, NO_2. OMPS as an independent measurement also plays a critical role in the global satellite constellation by providing a means of inter-calibrating and cross-validating with other satellite instruments (Judd et al., 2018). With the COVID-19 crisis, there is broad interest in accurate assessments of regional NO_2 column changes from multi-satellite platforms. The development of the first NOAA-20 OMPS NO_2 product describe herein was established after the emergence of the COVID-19 pandemic. In this study, we present the first results of NOAA-20 OMPS NO_2 with applications during the COVID-19 pandemic. We compare OMPS NO_2 retrievals with NO_2 columns retrieved from OMI and ground-based Pandora spectrometer measurements. Our results demonstrate OMPS capability in detecting spatial and temporal changes of tropospheric NO_2 air pollution.

2. NO_2 from NOAA-20

2.1. NOAA-20 OMPS instrument overview

OMPS Nadir Mapper (NM) is a nadir-viewing hyperspectral instrument that measures backscattered ultraviolet (UV) radiance spectra. The NOAA-20 OMPS spacecraft launched in November 2017, is the second of several OMPS missions planned for the next decade and beyond on the NOAA/NASA JPSS spacecrafts, with the first OMPS mission launched in October 2011, aboard SNPP spacecraft. Similar to SNPP, NOAA-20 is in a Sun-synchronous orbit with a local ascending (northbound) equator crossing-time at 1:30 p.m., close in time to the Aura/OMI & TROPOMI overpasses at 1:45 p.m. local time (Table 1). NOAA-20 OMPS has a spatial resolution of 17 × 13 km^2 at nadir, improved over the nadir resolution of 50 × 50 km^2 of SNPP OMPS, and OMPS resolution will be continually improved on the subsequent JPSS satellites.

NOAA-20 OMPS measures UV radiance in the 300–420 nm wavelength range at a spectral resolution of 1 nm and a sampling rate of 0.42 nm per pixel. Although NOAA-20 OMPS extends the spectral coverage to 420 nm (compared to SNPP OMPS in the 300–380 nm range), its radiance quality is poor for wavelength longer than 390 nm and thus not used for NO_2 retrieval, and the shorter wavelength spectra (<345 nm) are strongly affected by ozone absorption. Therefore, the 345–390 nm wavelength range was utilized for OMPS NO_2 retrieval, shorter in wavelength than other legacy UV/VIS instruments (Table 1). We adopted the Direct Vertical Column Fitting (DVCF) technique to retrieve NO_2 from NOAA-20 OMPS-NM UV radiance, which is the algorithm currently implemented in the operational SNPP OMPS NO_2 product (Yang et al., 2014). Details about the DVCF algorithm and challenges for NO_2 retrievals in the UV spectra are elucidated in section 2.2.

2.2. DVCF retrieval algorithm

The Direct Vertical Column Fitting (DVCF) algorithm is applied to the NOAA-20 OMPS-NM spectral measurements to retrieve the atmospheric NO2 vertical columns. The approach of this algorithm is to find retrieved parameters so that the modeled radiance spectra ($\boldsymbol{I_{TOA}}$) match the satellite-measured spectra ($\boldsymbol{I_m}$). Algebraically, radiance matching is accomplished by minimizing the cost function $\left|\boldsymbol{\Delta y}\ \mathbf{S_y}^{-\frac{1}{2}}\right|^2$, where $\boldsymbol{S_y}$ is the measurement error covariance matrix and $\boldsymbol{\Delta y} = \{\ln \boldsymbol{I_m} - \ln \boldsymbol{I_{TOA}}\}$ is the residual vector for all wavelengths in a spectral window, one of which at wavelength λ can be written as:

$$\boldsymbol{\Delta y}(\lambda) = \boldsymbol{V}\int_0^{\infty}\frac{\partial \ln \boldsymbol{I_{TOA}}(\lambda)}{\partial\, \boldsymbol{\tau_z}}\boldsymbol{S_z}\boldsymbol{\sigma}(\lambda, \boldsymbol{T_z})\boldsymbol{dz} - \sum_{i=1}^{m}\boldsymbol{\xi_i}\boldsymbol{\sigma_i}(\lambda,\ \boldsymbol{T_i}) + \sum_{k=0}^{n=1}\frac{\partial \ln \boldsymbol{I_{TOA}}(\lambda)}{\partial\, \boldsymbol{R}}\boldsymbol{\Delta R_k}(\lambda-\lambda_0)^k + \boldsymbol{\varepsilon} \quad (1)$$

The least-square solution to the set of Eq. (1) described the retrieval of NO_2 vertical column ($\boldsymbol{V}$) as a process of fitting the residuals with the vertical column weighting function (WF, i.e. $\int_0^{\infty}\frac{\partial \ln \boldsymbol{I_{TOA}}}{\partial \tau_z}\boldsymbol{S_z}\boldsymbol{\sigma}(\boldsymbol{T_z})\boldsymbol{dz}$) and the slant columns $\{\boldsymbol{\xi_i},\ \boldsymbol{i}=1\ldots\boldsymbol{m}\}$ of other trace gases (including O_3, HCHO, BrO, and OClO, thus m = 4) with their molecular absorption cross sections $\{\boldsymbol{\sigma_i}(\boldsymbol{T_i}),\ \boldsymbol{i}=1\ldots\boldsymbol{m}\}$ at their respective temperature $\{\boldsymbol{T_i},\ \boldsymbol{i}=1\ldots\boldsymbol{m}\}$. S_z is the shape factor, which is the normalized vertical profile; $\boldsymbol{T_z}$ is the

Table 1
Comparison of satellite NO_2 instruments on Low Earth Orbit, including OMI, SNPP OMPS, NOAA-20 OMPS and TROPOMI.

	OMI	SNPP OMPS	NOAA-20 OMPS	TROPOMI
Spectral window	405–465 nm	345–380 nm	345–390 nm	405–465 nm
Spectral resolution	0.63 nm	1 nm	1 nm	0.63 nm
Swath width	2600 km	2800 km	2800 km	2600 km
FOV	75°	110°	110°	75°
Signal-to-noise ratio	1200	2500	600–800[a]	1200
Nadir resolution	24 × 13 km^2	50 × 50 km^2	13 × 17 km^2	5.5 × 3.5 km^2
Overpassing time	13:45 LT	13:30 LT	13:30 LT	13:45 LT

[a] Note that the signal-to-noise ratio of NOAA-20 OMPS is estimated to be about $1/\sqrt{11}$ of that of SNPP OMPS.

atmospheric temperature, a function of altitude (z); and ε is the total error, which includes satellite measurement error and the forward modeling uncertainty. Here, $\boldsymbol{\tau_z}$ is the optical thickness of an infinitesimally thin layer at z, and the total absorption optical thickness($\boldsymbol{\tau}$) is the integration of $\boldsymbol{\tau_z}$: $\boldsymbol{\tau} = \int_0^\infty \boldsymbol{\tau_z} dz = V \int_0^\infty \boldsymbol{\sigma}(\boldsymbol{T_z})\, \boldsymbol{S_z}\, dz$. The radiance matching is primarily through adjusting the reflectivity parameters {R_k, k = 0 … n}, which specify the Mixed Lambert-Equivalent Reflectivity (MLER) model. Here n = 1 describes the reflectivity change linearly with wavelength, a simplified treatment to account for aerosol effects. The spectral structures in the measured spectra are then reproduced by finding the correct vertical column ($\boldsymbol{V}$) and other absorbers slant columns ($\boldsymbol{\xi_i}$).

After the direct retrieval of total vertical columns ($\boldsymbol{V}$) as described in Eq. (1), OMPS stratospheric and tropospheric NO_2 vertical columns are separated using an orbit-based sliding median correction approach. The basic premise behind Stratosphere-Troposphere Separation (STS) is that the spatial distribution of stratospheric NO_2 is more homogeneous than that of tropospheric NO_2 due to the localized anthropogenic emission and short lifetime of the latter. The sliding median STS technique used in NOAA-20 OMPS retrieval was first developed for SO_2 retrieval in OMI (Yang et al., 2007, 2009), and then applied in NO_2 retrieval in SNPP OMPS (Yang et al., 2014). It follows a simple procedure: first, retrieved total vertical columns are partitioned into stratospheric ($\boldsymbol{V_s^i}$) and tropospheric components using tropopause inputs and the a priori shape factors. Second, the initial stratospheric columns get refined by locating and smoothing out the high-frequency structures that are attributed to the inaccuracies in a priori shape factors. Specifically, two empirical latitudinal bands (e.g., 2° and 20°, subject to modifications in certain conditions) are used to construct two smoothed stratospheric fields from the initial field along the orbital track for each cross-track position of a satellite orbit using the sliding median method, as detailed in (Yang et al., 2014). The smaller latitude band is used to generate a higher-frequency smoothed field ($\boldsymbol{m_h}$) that retains possible tropospheric signals, while the larger band is used to construct a lower-frequency smoothed field ($\boldsymbol{m_l}$) with minimal tropospheric contributions that is representative of background median values. Thus, the excesses (+) and deficits (−) of stratospheric NO_2 are obtained from the difference between the two smoothed fields ($\boldsymbol{m_h} - \boldsymbol{m_l}$). The corrected stratospheric NO_2 column is then adjusted as $\boldsymbol{V_s} = \boldsymbol{V_s^i} - (\boldsymbol{m_h} - \boldsymbol{m_l})$. After the stratospheric vertical columns are consolidated, finally, the corresponding tropospheric NO_2 columns ($\boldsymbol{V_t}$) are retrieved by solving a new set of linear equations:

$$\ln\frac{\boldsymbol{I_m}(\lambda)}{\boldsymbol{I_{TOA}}(\lambda)} + \boldsymbol{V_s}\int_{\boldsymbol{Z_{tp}}}^{\infty} \boldsymbol{m_z}(\lambda)\boldsymbol{S_z}\boldsymbol{\sigma}(\lambda, \boldsymbol{T_z})d\boldsymbol{z} + \sum_i \boldsymbol{\xi_i}\boldsymbol{\sigma_i}(\lambda,\ \boldsymbol{T_i}) - \sum_{k=0}^{n}\frac{\partial \ln \boldsymbol{I_{TOA}}(\lambda)}{\partial\, \boldsymbol{R}}\boldsymbol{\Delta R_k}(\lambda-\lambda_0)^k = -\boldsymbol{V_t}\int_0^{\boldsymbol{Z_{tp}}} \boldsymbol{m_z}(\lambda)\boldsymbol{S_z}\boldsymbol{\sigma}(\lambda, \boldsymbol{T_z})d\boldsymbol{z} + \boldsymbol{\varepsilon} \quad (2)$$

where $\boldsymbol{Z_{tp}}$ is the tropopause altitude. This completes the whole process of DVCF retrieval of OMPS tropospheric and stratospheric NO_2 vertical columns.

The key improvement of the DVCF algorithm over the traditional Differential Optical Absorption Spectroscopy (DOAS) approach lies in the more accurate representation of NO_2 measurement sensitivity, and thus more accurate NO_2 retrieval. In UV, the Rayleigh scattering from air molecules is quite strong and varies with wavelength drastically (~1/λ^4). Consequently, the tropospheric air mass factors (AMFs) depend on the wavelength significantly. The spectrally dependent WF used in the DVCF captures the measurement sensitivity more accurately than the single-wavelength AMFs employed in the DOAS algorithm. Furthermore, retrieving surface reflectance or cloud fraction from the same spectral range, instead of taking it from ancillary inputs, such as climatological values or measurements from different spectra, improves the quantification of measurement sensitivity. Both improvements enable better spectral fits to the measured spectra and provide more accurate vertical column weighting functions, and thus allows more accurate and precise retrievals of NO_2 vertical columns than the traditional DOAS approach. Typically, the DOAS retrieval from UV spectra underestimates heavy NO_2 pollution (>2 DU) in the boundary layer by more than 10% compared to the corresponding DVCF retrieval.

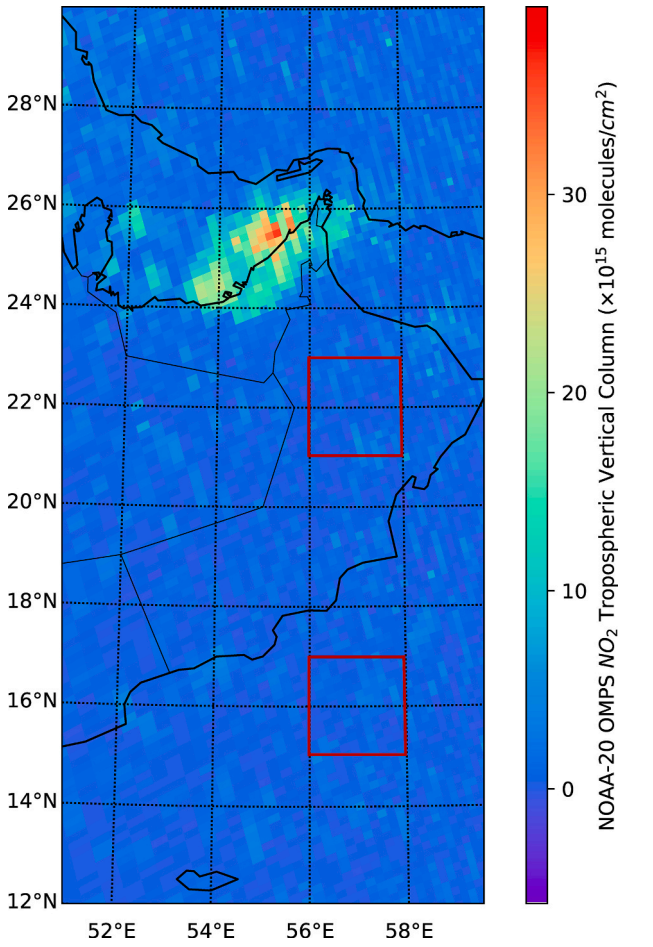

Fig. 1. NOAA-20 OMPS NO_2 tropospheric vertical columns over the Eastern Arabian Peninsula on November 10, 2019. The scan time on the map is 09:00 to 09:05 UTC. The sensitivity of NOAA-20 tropospheric NO_2 columns is reported over the remote ocean and desert, where red boxes indicate.

With the theoretical background of the DVCF algorithm, here we summarize the algorithmic procedure applied to NOAA-20 Level-1 (L1) data to produce the Level-2 (L2) NO_2 product in the flowchart Algorithm 1, including references to the input ancillary (Brodzik and Stewart, 2021) and climatological data (Kleipool et al., 2008; Yang and Liu, 2019).

Algorithm 1. Flowchart that shows the processing of NOAA-20 OMPS by the DVCF algorithm.

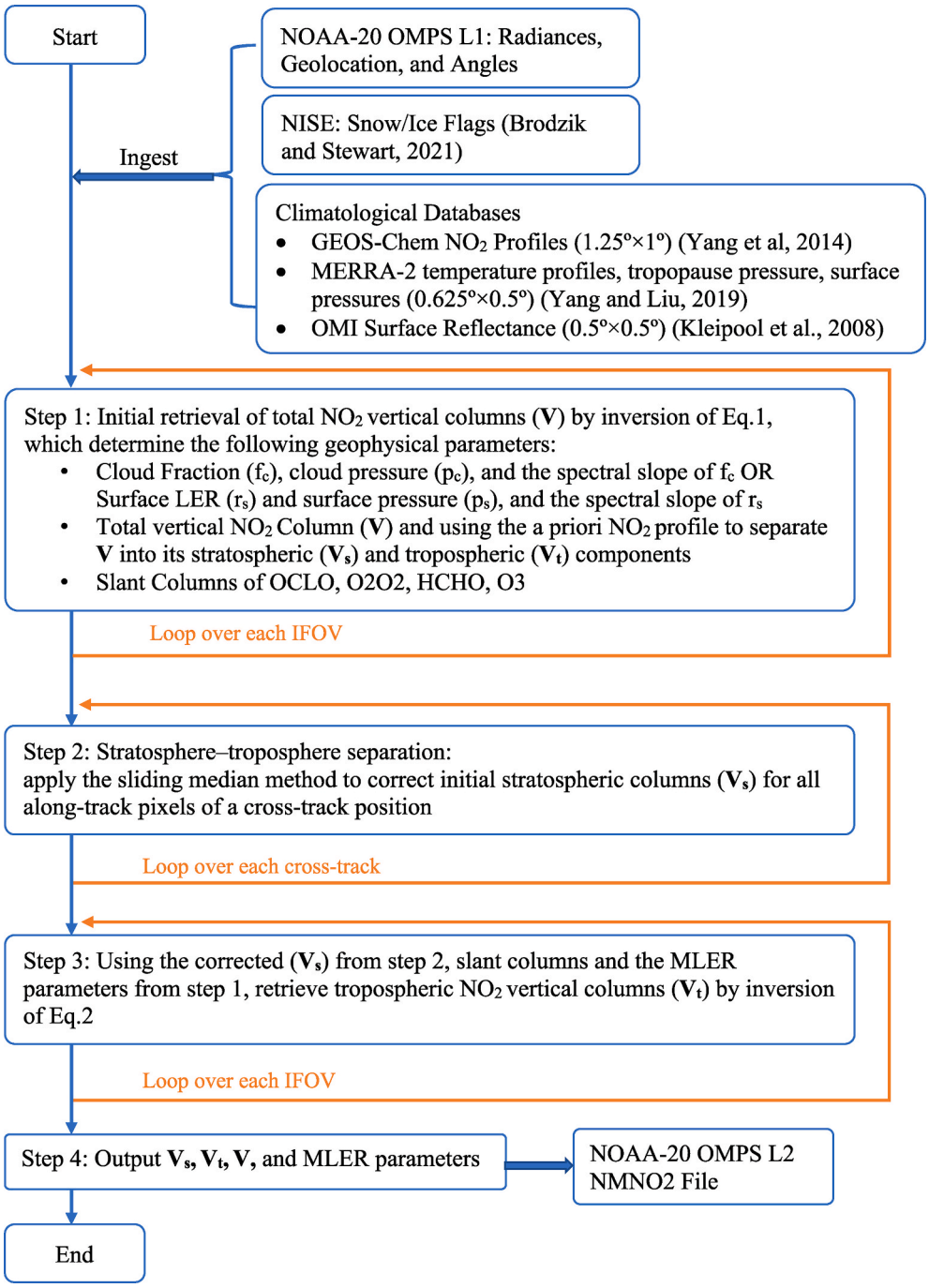

2.3. Measurement sensitivity of NOAA-20 OMPS NO_2

The precision (sensitivity) of a satellite instrument is often assessed over remote areas, where the measurement variability is dominated by random errors originating from measurement noise. The measurement sensitivity of NOAA-20 OMPS NO_2 tropospheric vertical column densities (TVCDs) over remote ocean (Indian Ocean) and remote desert (Arabian Peninsula) are 0.5×10^{15}, 0.7×10^{15} molecules/cm^2, respectively. The values are 1 σ (standard deviation) of the directly retrieved tropospheric NO_2 vertical columns (Fig. 1). We adopted the same method used to quantify OMI NO_2 sensitivity as demonstrated in (Boersma et al., 2007; Valin et al., 2011). The areas selected to report OMPS sensitivity are 2° by 2° boxes between 56°E and 58°E, the box for the remote desert over Arabian Peninsula is between 21°N and 23°N, and the box for the remote Indian ocean is between 15°N and 17°N (Fig. 1). It is worth noting that we used vertical columns to report sensitivity instead of the slant columns as used by ref (Valin et al., 2011). because the OMPS DVCF retrieval algorithm retrieves the vertical

columns directly from a spectral fit to the Earth reflectance spectrum. In other words, the slant column is a derived quantity from the vertical column retrieval. Therefore, it makes more sense to use vertical columns to characterize OMPS sensitivity. For OMI, since slant columns are determined with spectral fit in the first step of the DOAS retrieval algorithm, it is better to use slant column to quantify OMI sensitivity.

The sensitivity of SNPP OMPS NO_2 TVCDs is 0.4×10^{15} molecules/cm^2 (Yang et al., 2014), better than NOAA-20 OMPS. Although the two products are built on the same retrieval system, the NOAA-20 NO_2 is noisier than SNPP primarily because the NOAA-20 OMPS instrument has a smaller signal-to-noise ratio (SNR) than its predecessor SNPP OMPS (Table 1). Since SNPP OMPS has bigger pixel size (50×50 km^2) than NOAA-20 OMPS (17×13 km^2), if we were to estimate NOAA-20 SNR from SNPP, we can aggregate 11 NOAA-20 pixels into 1 SNPP pixel to make NOAA-20 equivalent to SNPP. This aggregation process cancels out noise but keeps the signal, which means that the NOAA-20 SNR is about $\sqrt{11}$ ~3.32 times lower than SNPP. Therefore, NOAA-20 OMPS measurement sensitivity is intrinsically limited by its smaller signal-to-noise ratio and the DVCF retrieval algorithm is specially designed to amplify its measurement sensitivity as possible.

3. Results

3.1. Stratospheric NO_2: comparison with OMI

Before evaluating NOAA-20 tropospheric NO_2 retrievals, we first examine the stratospheric NO_2 observations from NOAA-20, since the stratospheric columns represent the clean background values over which tropospheric NO_2 enhancements are detected. We compared the seasonal averaged NO_2 stratospheric vertical column densities (SVCDs) observed from NOAA-20 OMPS and OMI in Fig. 2. The daily NO_2 SVCDs (Level-2 data) collected from the two instruments were zonally averaged using 2° latitude bins for all cross-track iFOVs (OMI row anomaly affected pixels are excluded), and the seasonal averaged SVCDs were then plotted as a function of latitude. Since OMPS and OMI have similar overpassing time, the observed SVCDs are compared directly without photochemical corrections to compensate for NO_2 diurnal cycles (Rivas et al., 2014). In all seasons, the stratospheric NO_2 field is characterized by a tropical minimum over the equatorial NO_y (odd nitrogen) production zone, where total nitrogen is subject to upward and poleward transport. Outside the tropical regions, the stratospheric NO_2 field is characterized by a winter minimum and a summer maximum. The seasonal evolution of stratospheric NO_2 is explained by the sunlight-driven exchange between NO_x (nitrogen oxides) and other reservoir oxidized nitrogen species: N_2O_5 (primarily), HNO_3 and $ClONO_2$. As the amount of daily photolysis decreases over winter, NO_x begins to store into inactive N_2O_5 reservoirs, which results in a decrease of NO_x columns (Solomon and Garcia, 1983). Conversely, as the solar angle decreases in summer, the photolytic release of reservoir species increases NO_2 columns.

OMI and NOAA-20 OMPS retrievals of stratospheric NO_2 columns over the tropics and mid-latitude are very similar (Fig. 2). In high latitudes, the differences are larger. This is primarily due to the sunlight driven NO_2 diurnal variations at large solar zenith angles (SZA). The large SZA at higher latitude is more prone to the sharp NO_2 gradient at day-night transition, making direct column comparisons more difficult. In addition, large SZA increases the uncertainty in satellite retrieval of the NO_2 total columns due to stronger absorption in the stratosphere and lower signal-to-noise ratio. Studies found that the differences between satellite- and ground-based NO_2 measurements are generally larger for SZA above 45° (Ialongo et al., 2020). We have compared OMI cross-track positions that are not affected by row anomaly against the equivalent OMPS cross-track positions based on similar view zenith angle. We find that the row anomaly caused sampling mismatch are not the main reason for the large discrepancy at high latitudes.

OMPS and OMI stratospheric NO_2 columns show an agreement with $r = 0.96$ and average relative difference = −3% for the region between 65°S and 65°N. The excellent agreement between NOAA-20 OMPS and

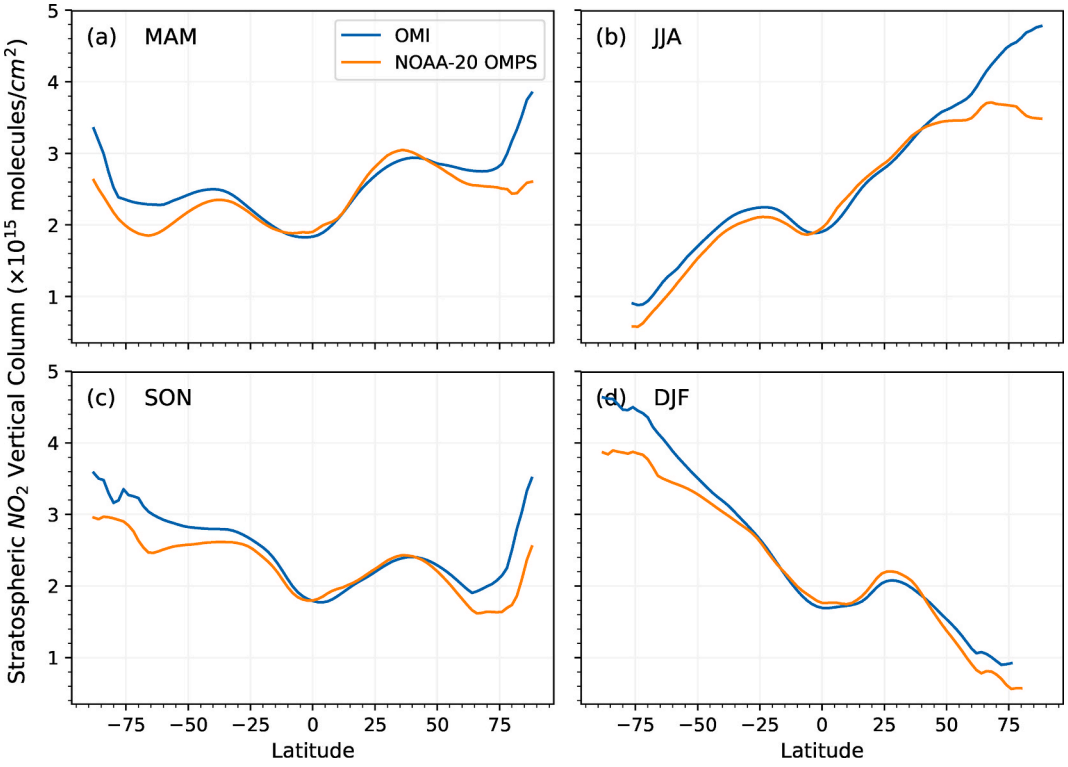

Fig. 2. Seasonal averaged stratospheric NO_2 vertical columns observed from NOAA-20 OMPS (orange curve) and OMI (blue curve) as a function of latitude for (a) MAM, (b) JJA, (c) SON, (d) DJF, over the period from 2019-03-01 to 2020-04-30. OMPS and OMI show excellent agreement with $r = 0.96$ and mean relative difference = −3% for the region between 65°S and 65°N. OMI pixels affected by row anomaly are excluded in the comparison.

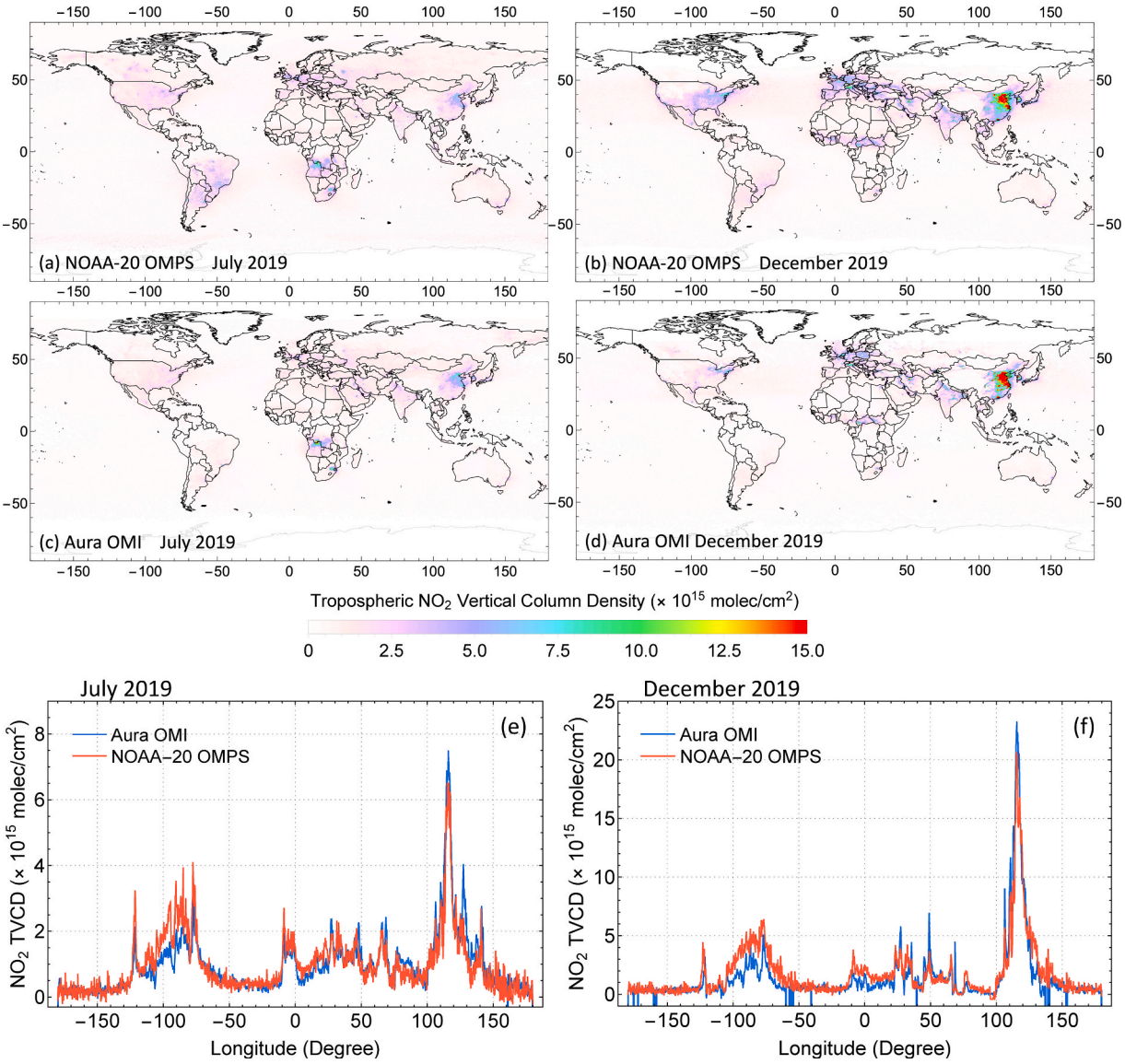

Fig. 3. Monthly averages of NO_2 tropospheric vertical column densities (TVCDs) observed by (**a, c**) NOAA-20 OMPS for July 2019 and (**b, d**) OMI for December 2019, pixels with cloud fraction of 30% and above are excluded. (**e, f**) Quantitative comparison of NOAA-20 OMPS and OMI monthly averaged NO_2 TVCDs at 38.625°N, from 180°W to 180°E.

OMI stratospheric columns is promising given that each relies on independent measurements and very different retrieval methodologies. Also, since stratospheric NO_2 is homogeneously distributed, this comparison is not subject to instrumental resolution difference.

3.2. *Tropospheric NO_2: comparison with OMI*

Fig. 3 shows maps of the gridded monthly mean NO_2 tropospheric vertical column densities (TVCDs) derived from NOAA-20 OMPS and OMI for July and December 2019. OMPS monthly mean NO_2 TVCDs are derived from OMPS Level-2 data and are compared directly with OMI monthly mean columns derived from OMI Level-2 data using identical gridding procedure. OMI and OMPS data are both gridded at 0.25° × 0.25° resolution, with the same cloud screening applied: iFOVs (pixels) with radiative cloud fraction >30% are excluded. OMI data affected by the row anomaly are also excluded. We computed OMPS and OMI monthly averages from respective Level-2 data in the following procedure: the value at each grid cell (0.25° × 0.25°) is determined by the weighted mean of the qualifying iFOVs that have overlap with the grid cell over the month. The weight is an observation coverage, defined as the ratio of GridCell-iFOV overlapping area to the iFOV area. The gridding strategy is often called 'oversampling' over a long temporal window, and we use the same gridding method to generate OMPS Level-3 data and calculate mean NO_2 TVCDs over the designated periods in Section 3.4.

The monthly maps provide perspectives of where persistent tropospheric NO_2 enhancements are located. Places like the United States East Coast, western Europe, East Asia, and northern India exhibit elevated NO_2 pollution, are the world's major industrial and densely populated regions. Both OMPS and OMI observe these NO_2 enhancements. To highlight the similarities and differences between the two NO_2 products, we plot the longitudinal variations of OMPS and OMI measurements in July and December 2019 mean TVCDs across 38.625°N, where the highest OMI monthly mean value is found in December 2019 (Fig. 3e and f). The NO_2 TVCDs from OMPS and OMI agree very well over China (between 100° and 140°) at this latitude, but OMPS TVCDs are higher than OMI over the U.S. (between −100° and −60°) and Europe (between −10° and 20°). These differences are likely due to different a priori profile assumptions over these regions. The a priori NO_2 profile used in the current NOAA-20 NO_2 product are taken from the monthly mean

profiles of a 2012 GEOS-Chem global simulation at a coarse resolution (1° latitude × 1.25° longitude). These a priori profiles describe a much higher boundary layer NO_2 concentrations than those of the more recent years. A higher boundary layer NO_2 in the a priori shape factors would result in higher NO_2 column retrievals. This potentially cause the higher OMPS column NO_2 retrievals than OMI in the U.S. and Europe. On the other hand, for China, although more recent-year a priori profiles might reflect lower NO_2 concentrations benefited from environmental regulations, there is still relatively large abundance of anthropogenic emissions near the surface compared to upper attitudes and thus the NO_2 vertical distributions (i.e., profile shapes) are not expected to change much. Therefore, the current agreement between OMPS and OMI in China would probably sustain in more recent-year a priori profiles. We are developing new a priori NO_2 profiles that are more appropriate for the current pollution levels to address the potential errors from inaccurate profile assumptions in the retrievals. Overall, the similar spatial patterns and good quantitative agreement demonstrate the high tropospheric NO_2 measurement sensitivity of NOAA-20 OMPS that is comparable to OMI.

3.3. Evaluating total NO_2 column with pandora ground-based observations

The accuracy of NOAA-20 OMPS NO_2 columns measurements was preliminarily evaluated against Pandora ground-based observations over the continental United States (U.S.) during the period from 2019-02-14 to 2020-04-30 (Fig. 5). Pandora instruments can retrieve NO_2 vertical column densities (VCDs) through two viewing geometries, either direct-sun or zenith sky. For the time of interest, 13 Pandora instruments operated in direct-sun mode over the U.S. are compared to NOAA-20 OMPS column measurements. The direct-sun mode Pandora instruments provide high-quality reference measurements for evaluating trace gas retrievals from satellite sensors due to their low uncertainties in AMFs (Judd et al., 2020). The ground stations used in this analysis cover a variety of atmospheric environments, including 4 Pandoras located in the New York City (NYC) region: Manhattan NY-CCNY, Queens NY, Bronx NY, and Bayonne NJ (Fig. 4b), and 9 other Pandoras located over mid-Atlantic and western U.S. states, representing urban/suburban/remote atmospheric conditions (Fig. 5). All the sites are operated as part of the Pandonia Global Network (PGN; www.pandonia-global-network.org). Only high-quality Pandora measurements with a quality flag of 0 or 10 were included in this analysis.

For the comparison between OMPS and Pandora NO_2 total vertical columns, we adopted the following coincidence criteria: 1) the average Pandora total NO_2 VCDs are calculated within ±30 min of OMPS overpass, and 2) all OMPS data have radiative cloud fractions less than 30%. The coincidence criteria are similar to those used in other validation studies (Ialongo et al., 2016; Judd et al., 2019). We calculated the linear regression statistics using Reduced Major Axis regression with correlation coefficient. This regression is chosen over Ordinary Least Square to recognize the potential errors/uncertainties in both evaluated and reference measurements. Note that the Ordinary Least Square statistics is also provided as a reference in Table 2. The difference and relative difference of the two column measurements are also calculated and analyzed, and are calculated in the following convention:

$$column\ difference = OMPS\ measurement - Pandora\ measurement \quad (3)$$

$$relative\ difference\ (\%) = \frac{column\ difference}{Pandora\ measurement} \times 100\% \quad (4)$$

Fig. 4a shows the scatter plot and linear regression statistics of OMPS and Pandora NO_2 total columns coincidences from 4 sites over NYC area (N = 283). NOAA-20 OMPS has an average low bias of 28% (median relative difference, Fig. S1b) and is moderately correlated (r = 0.45) with Pandora spectrometer measurements for the 4 NYC sites. The mean difference between OMPS and Pandora retrievals shows OMPS ubiquitously underestimates in the NYC region from -6.0×10^{15} (Queens NY) to -2.8×10^{15} (Bronx NY) molecules/cm^2 (Fig. 5). Outside of the NYC metro area, the average OMPS column NO_2 is generally higher than or close to Pandoras, with the mean difference between -0.3×10^{15} (Richmond CA) and 2.7×10^{15} (New Brunswick NJ) molecules/cm^2, except for New Haven CT, which OMPS underestimates with an average difference of -1.1×10^{15} molecules/cm^2 from Pandora (Fig. 5). To assess the statistical distribution of the OMPS biases, we plot the column NO_2 difference and percent difference as a function of pollution levels in Fig. 6. For the least polluted columns ($<3 \times 10^{15}$ molecules/cm^2), the inter-quantile range of column difference is 0.6–4.5 $\times 10^{15}$, with a median of 3.3×10^{15} molecules/cm^2. When pollution level increases, the median difference gradually shifts from positive towards negative. For the more polluted columns (12–15 and $>15 \times 10^{15}$ molecules/cm^2), the inter-quantile range of column differences are both in the negative range, with a median difference of -4 and -10×10^{15} molecules/cm^2,

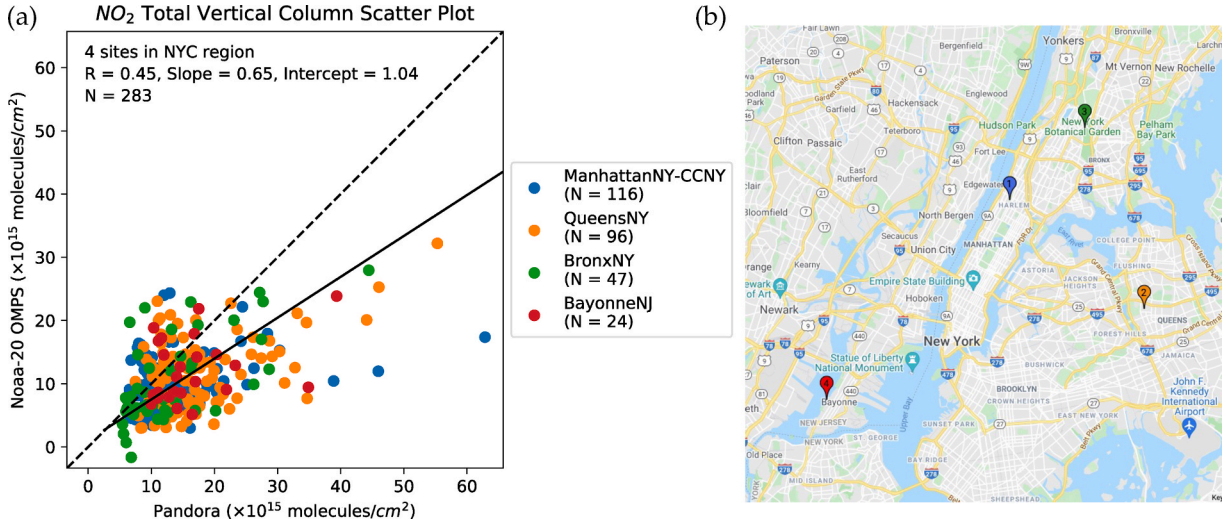

Fig. 4. (a) Scatter plot of NOAA-20 OMPS and Pandora observed NO_2 total vertical columns over 4 ground stations in New York metropolitan area, from 2019-02-14 to 2020-04-30. The statistics of linear regression fit are shown on the plot (N represents the number of coincidences). Note that different stations have different date spans and thus different number of coincidences with OMPS, coincidence by station is shown in the legend; (b) The locations of 4 stations on Google Map, the color of each station on the map corresponds to the color used in the scatter plot.

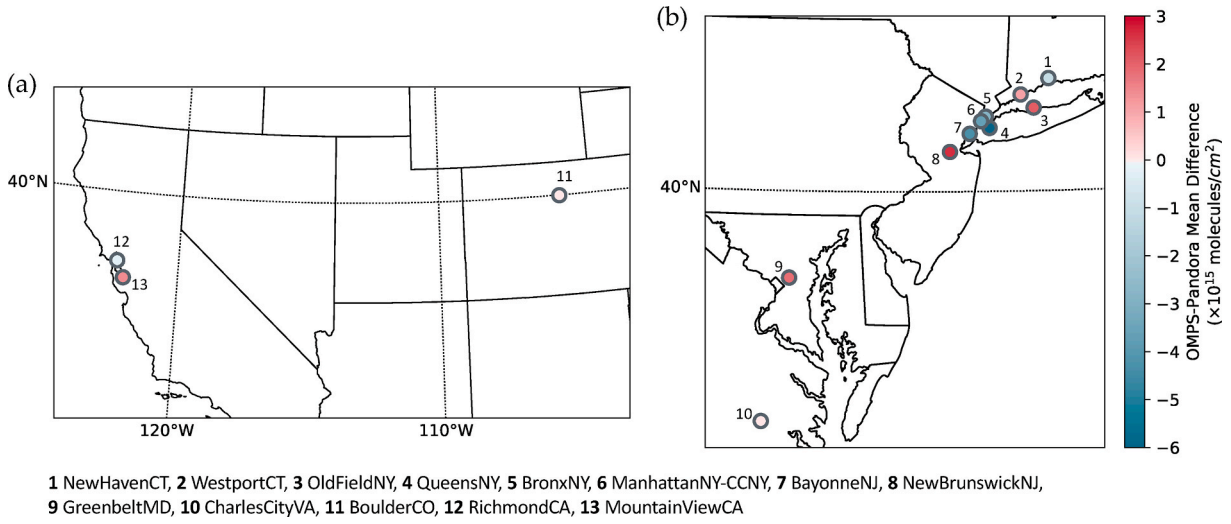

Fig. 5. Locations of Pandora ground stations over (a) western U.S. (3 stations) and (b) eastern U.S. (10 stations), colored by the average difference between OMPS and Pandora measured total NO_2 columns.

Table 2
Statistics of the comparison between NOAA-20 OMPS and Pandora NO_2 total columns, based on all data from 13 U.S. Pandora stations during 2019-02-14 to 2020-04-30. The uncertainties are the corresponding standard errors of the mean.

	Mean relative difference[a]	Mean difference[b]	Standard deviation of absolute bias[c]	r[d]	$slope_{OLS}$[e]	$slope_{RMA}$[f]	N[g]
All data	14.8 ± 2.0	−0.29 ± 0.15	5.8	0.40	0.32	0.81	1434
Pandora high[h]	−34.6 ± 2.1	−7.18 ± 0.49	7.4	0.43	0.29	0.72	225
Pandora low[i]	24.1 ± 2.2	1.00 ± 0.12	4.3	0.20	0.38	1.95	1209

[a] Mean relative difference (%).
[b] Mean difference (× 10^{15} molecules/cm^2).
[c] Standard deviation of column difference (× 10^{15} molecules/cm^2).
[d] Correlation coefficient.
[e] Least squares linear fit slope.
[f] Reduced major axis linear fit slope.
[g] Number of coincidences.
[h] Pandora NO_2 total columns≥12 × 10^{15} molecules/cm^2.
[i] Pandora NO_2 total columns <12 × 10^{15} molecules/cm^2.

respectively. Considering all data points from 13 sites during the 15-month validation span (N = 1434), the median difference and relative difference between NOAA-20 OMPS and Pandora are -0.1×10^{15} molecules/cm^2 and -1% respectively, with an inter-quantile range of -2.8 to 2.9×10^{15} molecules/cm^2 and -32%–44% respectively (Fig. 6). The overall linear correlation between NOAA-20 and Pandora total columns is 0.40 and the correlation is higher (r = 0.43) at higher pollution levels (Table 2). The quality of statistics of NOAA-20 OMPS is reasonably comparable to other satellite instrument bias with regard to Pandora measurements, see Text S1 for details (Herman et al., 2019; Ialongo et al., 2016, 2020; Judd et al., 2019; Lamsal et al., 2014).

These results from multiple Pandora spectrometer instruments indicate that OMPS NO_2 total columns underestimate for relatively large Pandora NO_2 total columns, corresponding to polluted urban regions and episodes of elevated pollution, while overestimate for relatively small NO_2 total columns. The low bias (OMPS underestimation) can be partially attributed to the sampling mismatch in spatial representativity between a point measurement from the ground-based spectrometer and an area-averaged quantity from the satellite iFOV (instantaneous Field of View, i.e., pixel). As the more polluted NO_2 columns observed by Pandora are likely occurring over spatial scales much smaller than the satellite resolutions, the satellite-to-Pandora linear relationship progressively worsens with increasing satellite pixel size, simply resulting from the flattening of higher NO_2 enhancement over larger spatial areas (Judd et al., 2019). Such behavior is more often associated with localized heterogeneous features rather than more well mixed regional-scale enhancements. In addition, because of the relatively coarse resolution of the OMPS a priori profiles, OMPS tropospheric columns are expected to have a low bias over polluted areas where the actual peak in the NO_2 profiles is close to the surface, and the boundary layer column is underestimated in the a priori. Similarly, the less polluted columns could be overestimated due to a slightly overestimate of boundary layer NO_2, resulting from the averaging effect of low-resolution a priori profiles in situations of large spatial heterogeneity. Replacing the coarse (1° × 1.25°) a priori NO_2 profiles with high-resolution profiles from chemical transport models can potentially improve the agreement between NOAA-20 OMPS and Pandora.

3.4. *Tropospheric NO_2 column reductions during COVID-19*

In this section, we demonstrate the high sensitivity of NOAA-20 OMPS NO_2 observations with COVID-19 application and quantify the impact of COVID-19 outbreak on global NO_2 pollution. During the early half of 2020, many countries around the world enforced physical distancing measures in response to the outbreak of the COVID-19 crisis (Table S1). China's policy interventions are among the most stringent. Fig. 7 shows a visual comparison of OMPS observed tropospheric NO_2 columns over China before and after the lockdown in 2020 (a-e) and over the same period in 2021 (f-j), with indications of the Chinese New Year holiday (by red lantern, top left) and of the lockdown period (by padlock, bottom right). In 2021, OMPS observed large winter NO_2 abundances (Fig. 7f and g) followed by a drop during the Chinese New

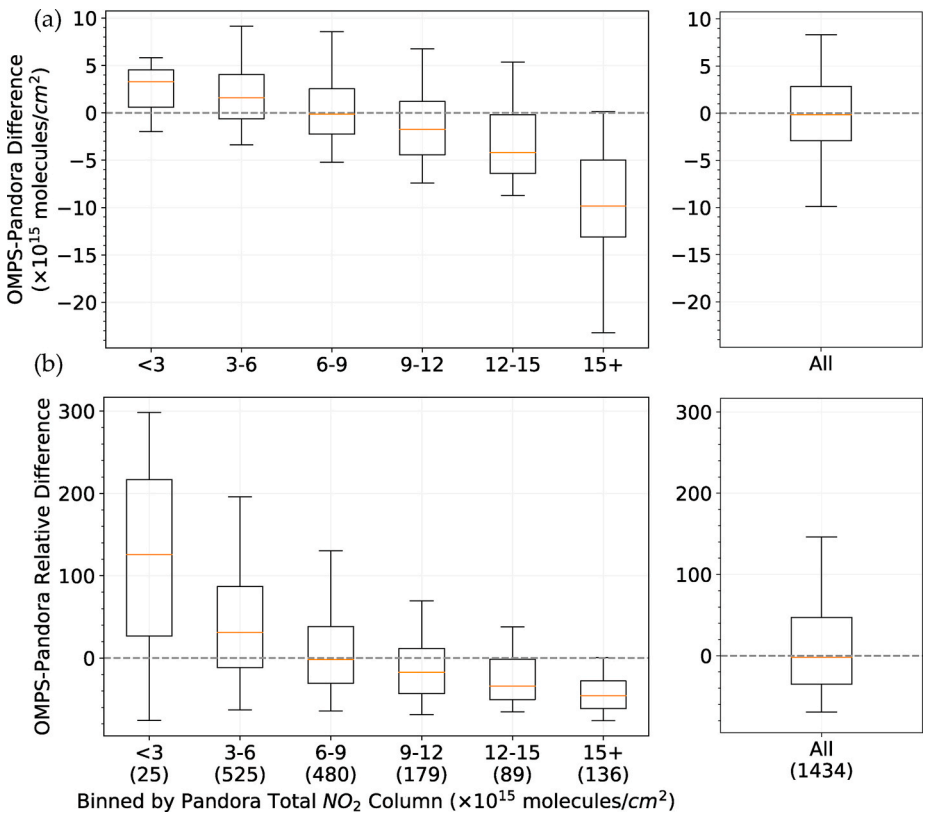

Fig. 6. Box-whisker plots (95-75-50-25-5 percentiles) showing the (a) absolute difference and (b) relative difference between NOAA-20 OMPS and Pandora measured total NO_2 columns, binned by Pandora columns at the labeled thresholds (left), as well as all data points (right). The number of points in each bin and all data are indicated by the numbers in parentheses. The data used in the analysis are collected from the 13 U.S. Pandora stations as shown in Fig. 5, over a period from 2019-02-14 to 2020-04-30.

Year holiday (CNY hereafter, Fig. 7h). The NO_2 TVCDs decline during CNY is a typical phenomenon observed every year because most Chinese factories shut down for the holiday and the traffic volumes decrease, resulting in a decrease in fuel consumption and thus NO_x emissions. A rebound of NO_2 TVCDs is usually observed right after CNY, marking the end of the 7-day CNY holiday and people get back to work (Fig. 7i). Note that the NO_2 rebound after CNY is much lower than its January peak, due to seasonality caused by shorter NO_2 lifetime in the warmer season. In 2020, since the initial phase lockdown is coincident with the CNY holiday, NO_x emissions curtail significantly and NOAA-20 OMPS observations indicate a steep drop of NO_2 TVCDs, reaching a factor of 2 or more at most Chinese cities (Fig. 7b). The average NO_2 reduction in 2020 over China is 35% from "before" (Fig. 7a) to "after" (Fig. 7b), while a reduction of 15% in 2021 is observed. This suggests that the observed reduction in 2020 far exceeds the typical holiday-related reduction. In addition, unlike the typical years that we see a clear NO_2 reduction during and a quick increase after CNY, NO_2 columns do not bounce back after the week of 2020 CNY holiday (Fig. 7c). In fact, it remains low for several weeks during strict COVID-19 quarantine (Jan 31 – Feb 17, 2020), after which NO_2 columns gradually recover, reflecting the return of economic activities and NO_x emissions (Fig. 7d and e).

A quantitative analysis of the impact of the COVID-19 measures on NO_2 in China as well as in other countries is given in Table 3. Note that the relatively large and not fully understood contribution of background NO_2 columns has a large impact on trend analyses as more background signal is incorporated into the analysis, whether by incorporating a large spatial area or by computing the analysis over less polluted cities (Qu et al., 2021; Silvern et al., 2019). We compare the observed NO_2 TVCDs during the lockdown in 2020 versus a recovering year NO_2 in 2021. This year-over-year comparison calculates NO_2 column averages starting on the same reference date and last for 21 days, to exclude seasonality-caused NO_2 changes. For the Chinese cities in Table 3, we averaged NO_2 TVCDs between January 31 and February 10, 2020 (11 days) compared to the same period in 2021, in order to eliminate the interference of CNY holidays. Similarly, the lockdown period for Iran was chosen between 4 March and 19 March (16 days) to eliminate the interference of the Nowruz holiday. Substantial NO_2 column reductions in 2020 (relative to 2021) are evident in many cities around the world where strict COVID-19 precautions were enforced. The observed column decreases are largely due to the decline of traffic emissions, by far the dominant NO_x emission source in cities, as well as decreases in industrial activities and power generation (Myllyvirta, 2020; Schuman, 2020; Zara, 2020). Simulations of chemistry transport models are needed if to isolate the benefit of emission reduction from variations of transport (Valin et al., 2013) or NO_x lifetime (Laughner and Cohen, 2019). Note that since we are comparing 2020 NO_2 columns to 2021, part of the lockdown related NO_2 reduction might be canceled out by the lower emission rate in 2021 due to the emission declines benefited from environmental regulations with each advancing year (Wu et al., 2019). Therefore, the actual NO_2 decreases could be larger if we were to compare with 2019 NO_2, as shown in the TROPOMI study of (Bauwens et al., 2020) Table 1.

4. Summary

In this work, we have presented a suite of product development behind the new NOAA-20 OMPS tropospheric NO_2 columns, covering retrieval algorithm, validation, and application during COVID-19. We applied the advanced DVCF algorithm and effective STS approach to UV measurements from NOAA-20/OMPS NM, which were successfully used to retrieve NO_2 from its predecessors: SNPP/OMPS and Aura/OMI.

To evaluate NOAA-20 OMPS NO_2 column retrievals, we first compared the stratospheric NO_2 vertical columns derived from OMPS to those from OMI. The comparison shows excellent agreement in detecting the stratospheric background columns between the two instruments, which facilitates the accuracy of the remained OMPS tropospheric NO_2 retrievals. The result also validates the sliding-median STS scheme that is adopted in NOAA-20 OMPS, especially given the agreement relies on

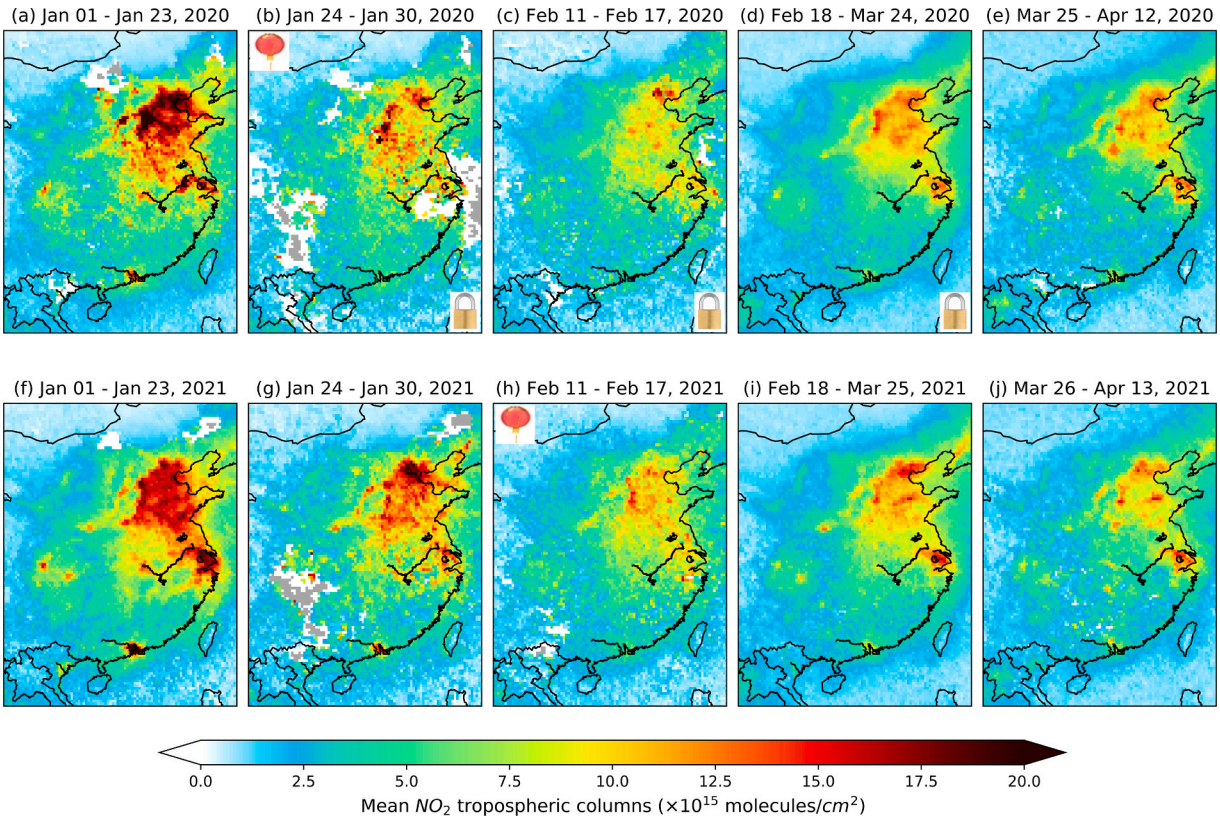

Fig. 7. Mean tropospheric NO_2 columns over China as observed by NOAA-20 OMPS (**a**) before and (**b-e**) after the COVID-19 lockdowns. For the comparison, the same time periods are shown for 2021 (**f-j**). The Chinese New Year holiday covers the weeks of Jan 24–30 in 2020 and Feb 11–17 in 2021, which are indicated by the red lanterns in panel (**b**) and (**h**). The lockdown measures are initiated during and extended after the 2020 Chinese New Year holiday, shown by the padlock sign in panel (**b-d**), and partial loosening of the restrictions starting Mar 25, 2020, shown in panel (**e**). Grey areas on the maps indicate no valid data due to the 30% cloud fraction filter.

Table 3
NO_2 TCVDs reduction observed during the COVID-19 lockdown period, starting on the Reference date and lasting for 21 days, relative to the same period in 2021, with the exception of China and Iran, where it lasts for 11 and 16 days respectively, in order to avoid the interference with the New Year Holidays. The percentage change is defined as ($TVCDs_{2020}$ - $TVCDs_{2021}$)/$TVCDs_{2021}$ × 100%. The numbers in the brackets are standard error of the mean.

City	Lat	Lon	Reference date	NOAA-20 OMPS
Beijing	39.9	116.4	31-Jan-20	−27(±4)%
Tianjin	39.3	117.4	31-Jan-20	−33(±3)%
Shenyang	41.8	123.4	31-Jan-20	−21(±4)%
Zhengzhou	34.7	113.6	31-Jan-20	−29(±3)%
Jinan	36.7	117.1	31-Jan-20	−46(±3)%
Shanghai	31.2	121.5	31-Jan-20	3(±7)%
Chengdu	30.6	104.1	31-Jan-20	−50(±6)%
Guangzhou	23.1	113.3	31-Jan-20	−68(±3)%
Shenzhen	22.5	114.1	31-Jan-20	−56(±4)%
Hong Kong	22.3	114.2	31-Jan-20	−54(±4)%
New Delhi	28.6	77.2	25-Mar-20	−16(±2)%
Mumbai	19.1	72.9	25-Mar-20	−12(±4)%
Milan	45.5	9.2	23-Feb-20	−23(±4)%
Venice	45.4	12.3	23-Feb-20	−16(±4)%
Madrid	40.4	3.7	15-Mar-20	−32(±3)%
Barcelona	41.4	2.2	15-Mar-20	−15(±4)%
Moscow	55.8	37.6	30-Mar-20	−37(±3)%
Tehran	35.7	51.4	04-Mar-20	12(±7)%
New York	40.7	−74.0	24-Mar-20	−22(±4)%
Washington DC	38.9	−77.0	24-Mar-20	−18(±4)%
Chicago	41.9	−87.6	24-Mar-20	−17(±4)%

Note: We used OMPS global daily gridded Level-3 data at 0.25° × 0.25° and the reductions are calculated based on pixels within a 100-km radius around the city center with cloud fractions of 40% or less.

independent spectral measurements at different wavelengths using very different retrieval methods. We compared NOAA-20 OMPS with OMI monthly mean TVCDs observations for December 2019. It shows similar spatial distributions and good quantitative agreement. We then preliminarily validated OMPS NO_2 columns against the independent NO_2 measurements from 4 ground-based Pandora spectrometers over the NYC metro area. NOAA-20 NO_2 observations biased low against (−28%) and are moderately correlated (r = 0.45) with Pandora total columns. The evaluation was then extended to other U.S. Pandora stations, with a total of 13 stations compared with NOAA-20 OMPS. The results suggest that OMPS NO_2 total columns underestimate for relatively large Pandora NO_2 total columns, corresponding to polluted urban regions and episodes of elevated pollution, while overestimate for relatively small NO_2 total columns. Part of the low biases is expected and can be explained by spatial representativity mismatch between satellite and ground-based measurements, when an area-averaged quantity over relatively large satellite pixel is compared with Pandora observations that have small FOV. Such kind of spatial representativity mismatch is often associated with localized large pollution enhancements observed by Pandora and OMPS is spatially averaged with nearby less-polluted locations within the larger satellite pixel area. Other than that, the biases (both underestimation and overestimation) are possibly caused by the coarse a priori profiles currently used in the NOAA-20 NO_2 retrievals. Replacing the a priori NO_2 profiles from high-resolution chemical transport models could potentially improve the agreement. Finally, with the new NOAA-20 OMPS NO_2 retrievals, we investigated the impact of COVID-19 lockdown on urban NO_2 air pollution. It shows a 20–40% drastic decline in tropospheric NO_2 around the world in January–April 2020 during COVID-19 precautions, supporting the analyses from other satellite-based studies (Bauwens et al., 2020; Goldberg et al., 2020; Liu

et al., 2020). These results demonstrate the high sensitivity of NOAA-20 OMPS to tropospheric NO_2 and validate its potential use for extending the long-term global NO_2 record on the series of OMPS-NMs aboard JPSS satellites.

Disclaimer

The scientific results and conclusions, as well as any views or opinions expressed herein, are those of the author(s) and do not necessarily reflect those of EPA, NOAA, or the Department of Commerce.

CRediT authorship contribution statement

Xinzhou Huang: Conceptualization, Data curation, Formal analysis, Investigation, Methodology, Software, Validation, Visualization, Writing – original draft, Writing – review & editing. **Kai Yang:** Conceptualization, Data curation, Funding acquisition, Methodology, Project administration, Resources, Software, Supervision, Writing – review & editing. **Shobha Kondragunta:** Project administration, Resources, Supervision, Writing – review & editing. **Zigang Wei:** Investigation. **Lukas Valin:** Resources, Writing – review & editing. **James Szykman:** Resources, Supervision, Writing – review & editing. **Mitch Goldberg:** Project administration, Resources, Supervision.

Declaration of competing interest

The authors declare that they have no known competing financial interests or personal relationships that could have appeared to influence the work reported in this paper.

Data Availability Statement

The NOAA-20 OMPS NO2 data can be obtained at https://umd.box.com/v/n20-omps-no2. Pandora data are located at http://data.pandonia-global-network.org/, and OMI L2 NO2 data at https://disc.gsfc.nasa.gov/datasets/OMNO2_003/summary.

Acknowledgement

This work was supported by the U.S. National Oceanic and Atmospheric Administration.

(NOAA) [grant number: NA19NES4320002]. We acknowledge the JPSS project for providing the OMPS L1 data used in this study.

Appendix A. Supplementary data

Supplementary data to this article can be found online at https://doi.org/10.1016/j.atmosenv.2022.119367.

References

Bauwens, M., Compernolle, S., Stavrakou, T., Müller, J.F., van Gent, J., Eskes, H., Levelt, P.F., van der A, R., Veefkind, J.P., Vlietinck, J., Yu, H., Zehner, C., 2020. Impact of coronavirus outbreak on NO2 pollution assessed using TROPOMI and OMI observations. Geophys. Res. Lett. 47, 1–9. https://doi.org/10.1029/2020GL087978.

Beirle, S., Boersma, K.F., Platt, U., Lawrence, M.G., Wagner, T., 2011. Megacity emissions and lifetimes of nitrogen oxides probed from space. Science 333 (80-), 1737–1739. https://doi.org/10.1126/SCIENCE.1207824.

Beirle, S., Borger, C., Dörner, S., Li, A., Hu, Z., Liu, F., Wang, Y., Wagner, T., 2019. Pinpointing nitrogen oxide emissions from space. Sci. Adv. 5, 1–7. https://doi.org/10.1126/sciadv.aax9800.

Boersma, K.F., Eskes, H.J., Veefkind, J.P., Brinksma, E.J., Van Der A, R.J., Sneep, M., Van Den Oord, G.H.J., Levelt, P.F., Stammes, P., Gleason, J.F., Bucsela, E.J., 2007. Near-real time retrieval of tropospheric NO2 from OMI. Atmos. Chem. Phys. 7, 2103–2118. https://doi.org/10.5194/acp-7-2103-2007.

Brodzik, M.J., Stewart, J.S., 2021. Near-Real-Time SSM/I-SSMIS EASE-Grid Daily Global Ice Concentration and Snow Extent. NASA National Snow and Ice Data Center Distributed Active Archive Center, Boulder, Colorado USA. https://doi.org/10.5067/JAQDJKPX0S60. Version 3 [Data Set]. (Accessed 8 September 2022).

Duncan, B.N., Lamsal, L.N., Thompson, A.M., Yoshida, Y., Lu, Z., Streets, D.G., Hurwitz, M.M., Pickering, K.E., 2016. A space-based, high-resolution view of notable changes in urban NOx pollution around the world (2005–2014). J. Geophys. Res. 121, 976–996. https://doi.org/10.1002/2015JD024121.

ESA, 2020. Air pollution drops in India following lockdown. Eur. Space Agency (Brochure) ESA Br. 1–5.

Goldberg, D.L., Anenberg, S.C., Griffin, D., McLinden, C.A., Lu, Z., Streets, D.G., 2020. Disentangling the impact of the COVID-19 lockdowns on urban NO2 from natural variability. Geophys. Res. Lett. 47 https://doi.org/10.1029/2020GL089269.

Herman, J., Abuhassan, N., Kim, Jhoon, Kim, Jae, Dubey, M., Raponi, M., Tzortziou, M., 2019. Underestimation of column NO2 amounts from the OMI satellite compared to diurnally varying ground-based retrievals from multiple PANDORA spectrometer instruments. Atmos. Meas. Tech. 12, 5593–5612. https://doi.org/10.5194/amt-12-5593-2019.

Huang, G., Sun, K., 2020. Non-negligible impacts of clean air regulations on the reduction of tropospheric NO2 over East China during the COVID-19 pandemic observed by OMI and TROPOMI. Sci. Total Environ. 745, 141023 https://doi.org/10.1016/j.scitotenv.2020.141023.

Ialongo, I., Herman, J., Krotkov, N., Lamsal, L., Folkert Boersma, K., Hovila, J., Tamminen, J., 2016. Comparison of OMI NO2 observations and their seasonal and weekly cycles with ground-based measurements in Helsinki. Atmos. Meas. Tech. 9, 5203–5212. https://doi.org/10.5194/amt-9-5203-2016.

Ialongo, I., Virta, H., Eskes, H., Hovila, J., Douros, J., 2020. Comparison of TROPOMI/Sentinel-5 Precursor NO2 observations with ground-based measurements in Helsinki. Atmos. Meas. Tech. 13, 205–218. https://doi.org/10.5194/amt-13-205-2020.

Judd, L.M., Al-Saadi, J.A., Janz, S.J., Kowalewski, M.J.G., Bradley Pierce, R., Szykman, J. J., Valin, L.C., Swap, R., Cede, A., Mueller, M., Tiefengraber, M., Abuhassan, N., Williams, D., 2019. Evaluating the impact of spatial resolution on tropospheric NO2 column comparisons within urban areas using high-resolution airborne data. Atmos. Meas. Tech. 12, 6091–6111. https://doi.org/10.5194/amt-12-6091-2019.

Judd, L.M., Al-Saadi, J.A., Szykman, J.J., Valin, L.C., Janz, S.J., Kowalewski, M.G., Eskes, H.J., Pepijn Veefkind, J., Cede, A., Mueller, M., Gebetsberger, M., Swap, R., Bradley Pierce, R., Nowlan, C.R., González Abad, G., Nehrir, A., Williams, D., 2020. Evaluating sentinel-5P TROPOMI tropospheric NO2 column densities with airborne and Pandora spectrometers near New York city and long island sound. Atmos. Meas. Tech. 13, 6113–6140. https://doi.org/10.5194/AMT-13-6113-2020.

Judd, L.M., Al-Saadi, J.A., Valin, L.C., Bradley Pierce, R., Yang, K., Janz, S.J., Kowalewski, M.G., Szykman, J.J., Tiefengraber, M., Mueller, M., 2018. The dawn of geostationary air quality monitoring: case studies from Seoul and Los Angeles. Front. Environ. Sci. 6 https://doi.org/10.3389/fenvs.2018.00085.

Kleipool, Q.L., Dobber, M.R., de Haan, J.F., Levelt, P.F., 2008. Earth surface reflectance climatology from 3 years of OMI data. J. Geophys. Res. Atmos. 113, 18308 https://doi.org/10.1029/2008JD010290.

Kondragunta, S., Wei, Z., McDonald, B.C., Goldberg, D.L., Tong, D.Q., 2021. COVID-19 induced fingerprints of a new normal urban air quality in the United States. J. Geophys. Res. Atmos. 126, e2021JD034797 https://doi.org/10.1029/2021JD034797.

Lamsal, L.N., Krotkov, N.A., Celarier, E.A., Swartz, W.H., Pickering, K.E., Bucsela, E.J., Gleason, J.F., Martin, R.V., Philip, S., Irie, H., Cede, A., Herman, J., Weinheimer, A., Szykman, J.J., Knepp, T.N., 2014. Evaluation of OMI operational standard NO2 column retrievals using in situ and surface-based NO2 observations. Atmos. Chem. Phys. 14, 11587–11609. https://doi.org/10.5194/acp-14-11587-2014.

Laughner, J.L., Cohen, R.C., 2019. Direct observation of changing NOx lifetime in North American cities. Science 366 (80-), 723–727. https://doi.org/10.1126/science.aax6832.

Lelieveld, J., Evans, J.S., Fnais, M., Giannadaki, D., Pozzer, A., 2015. The contribution of outdoor air pollution sources to premature mortality on a global scale. Nature 525, 367–371. https://doi.org/10.1038/nature15371.

Lin, N., Wang, Y., Zhang, Y., Yang, K., 2019. A large decline of tropospheric NO2 in China observed from space by SNPP OMPS. Sci. Total Environ. 675, 337–342. https://doi.org/10.1016/j.scitotenv.2019.04.090.

Liu, F., Page, A., Strode, S.A., Yoshida, Y., Choi, S., Zheng, B., Lamsal, L.N., Li, C., Krotkov, N.A., Eskes, H., Ronald van der, A., Veefkind, P., Levelt, P.F., Hauser, O.P., Joiner, J., 2020. Abrupt decline in tropospheric nitrogen dioxide over China after the outbreak of COVID-19. Sci. Adv. 6, 1–10. https://doi.org/10.1126/sciadv.abc2992.

Myllyvirta, L., 2020. Analysis: Coronavirus Temporarily Reduced China's CO2 Emissions by a Quarter [WWW Document]. Carbonbrief. URL. https://www.carbonbrief.org/analysis-coronavirus-has-temporarily-reduced-chinas-co2-emissions-by-a-quarter, 10.2.21.

Qu, Z., Jacob, D.J., Silvern, R.F., Shah, V., Campbell, P.C., Valin, L.C., Murray, L.T., 2021. US COVID-19 shutdown demonstrates importance of background NO2 in inferring NOx emissions from satellite NO2 observations. Geophys. Res. Lett. 48, 1–8. https://doi.org/10.1029/2021GL092783.

Rivas, M.B., Veefkind, P., Boersma, F., Levelt, P., Eskes, H., Gille, J., 2014. Intercomparison of daytime stratospheric NO2 satellite retrievals and model simulations. Atmos. Meas. Tech. 7, 2203–2225. https://doi.org/10.5194/amt-7-2203-2014.

Schuman, R., 2020. INRIX U.S. National Traffic Volume Synopsis [WWW Document]. INRIX. URL. https://inrix.com/blog/covid19-us-traffic-volume-synopsis/, 10.2.21.

Seinfeld, J.H., Pandis, S.N., 2016. Atmospheric Chemistry and Physics: from Air Pollution to Climate Change, third ed. Wiley.

Shah, V., Jacob D, J., Li, K., Silvern, R., Zhai, S., Liu, M., Lin, J., Zhang, Q., 2020. Effect of changing NOx lifetime on the seasonality and long-term trends of satellite-observed tropospheric NO2 columns over China. Atmos. Chem. Phys. 20, 1483–1495. https://doi.org/10.5194/acp-20-1483-2020.

Silvern, R.F., Jacob, D.J., Mickley, L.J., Sulprizio, M.P., Travis, K.R., Marais, E.A., Cohen, R.C., Laughner, J.L., Choi, S., Joiner, J., 2019. Using Satellite Observations of Tropospheric NO2 Columns to Infer Long-Term Trends in US NOx Emissions: the Importance of Accounting for the Free Tropospheric NO2 Background 19, pp. 1–16. https://doi.org/10.5194/acp-19-8863-2019.

Solomon, S., Garcia, R.R., 1983. On the distribution of nitrogen dioxide in the high-latitude stratosphere. J. Geophys. Res. Ocean. 88, 5229–5239. https://doi.org/10.1029/JC088IC09P05229.

Tzortziou, M., Kwong, C.F., Goldberg, D., Schiferl, L., Commane, R., Abuhassan, N., Szykman, J., Valin, L., 2021. Declines and peaks in NO_2 pollution during the multiple waves of the COVID-19 pandemic in the New York metropolitan area. Atmos. Chem. Phys. Discuss. 1–30. https://doi.org/10.5194/acp-2021-592.

Valin, L.C., Russell, A.R., Bucsela, E.J., Veefkind, J.P., Cohen, R.C., 2011. Observation of slant column NO 2 using the super-zoom mode of AURA-OMI. Atmos. Meas. Tech. 4, 1929–1935. https://doi.org/10.5194/amt-4-1929-2011.

Valin, L.C., Russell, A.R., Cohen, R.C., 2013. Variations of OH radical in an urban plume inferred from NO2 column measurements. Geophys. Res. Lett. 40, 1856–1860. https://doi.org/10.1002/GRL.50267.

Wu, R., Liu, F., Tong, D., Zheng, Y., Lei, Y., Hong, C., Li, M., Liu, J., Zheng, B., Bo, Y., Chen, X., Li, X., Zhang, Q., 2019. Air quality and health benefits of China's emission control policies on coal-fired power plants during 2005–2020. Environ. Res. Lett. 14, 094016 https://doi.org/10.1088/1748-9326/ab3bae.

Yang, K., Carn, S.A., Ge, C., Wang, J., Dickerson, R.R., 2014. Advancing measurements of tropospheric NO2 from space: new algorithm and first global results from OMPS. Geophys. Res. Lett. 41, 4777–4786. https://doi.org/10.1002/2014GL060136.

Yang, K., Krotkov, N.A., Krueger, A.J., Carn, S.A., Bhartia, P.K., Levelt, P.F., 2009. Improving retrieval of volcanic sulfur dioxide from backscattered UV satellite observations L03102. Geophys. Res. Lett. 36, 1–5. https://doi.org/10.1029/2008GL036036.

Yang, K., Krotkov, N.A., Krueger, A.J., Carn, S.A., Bhartia, P.K., Levelt, P.F., 2007. Retrieval of large volcanic SO2 columns from the Aura ozone monitoring instrument: comparison and limitations. J. Geophys. Res. Atmos. 112 https://doi.org/10.1029/2007JD008825.

Yang, K., Liu, X., 2019. Ozone profile climatology for remote sensing retrieval algorithms. Atmos. Meas. Tech. Discuss. 1–39. https://doi.org/10.5194/amt-2019-116.

Zara, C., 2020. Watch Flight Traffic Literally Disappear from the Skies as the Coronavirus Hits Travel Demand [WWW Document]. Fastcompany. URL. https://www.fastcompany.com/90473146/watch-flight-traffic-literally-disappear-from-the-skies-as-the-coronavirus-hits-travel-demand, 10.2.21.